ARTICLE

Photobase-Triggered Formation of 3D Epitaxially Fused Quantum Dot Superlattices with High Uniformity and Low Bulk Defect Densities

Caroline Qian, Alex Abelson, Anneka Miller-Casas, Robert Capp, Ilya Vinogradov, Nina S. Udagawa, Nien-Hui Ge, and Matt Law*

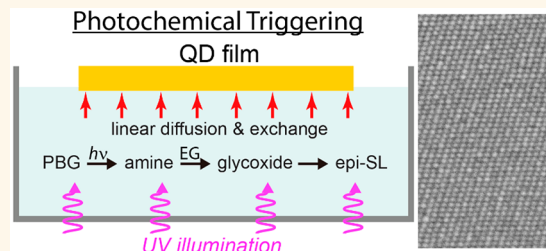Read Online

ACCESS | Metrics & More | Article Recommendations | Supporting Information

ABSTRACT: Highly ordered epitaxially fused colloidal quantum dot (QD) superlattices (epi-SLs) promise to combine the size-tunable photophysics of QDs with the efficient charge transport of bulk semiconductors. However, current epi-SL fabrication methods are crude and result in structurally and chemically inhomogeneous samples with high concentrations of extended defects that localize carriers and prevent the emergence of electronic mini-bands. Needed fabrication improvements are hampered by inadequate understanding of the ligand chemistry that causes epi-SL conversion from the unfused parent SL. Here we show that epi-SL formation by the conventional method of amine injection into an ethylene glycol subphase under a floating QD film occurs by deprotonation of glycol by the amine and subsequent exchange of oleate by glycoxide on the QD surface. By replacing the amine with hydroxide ion, we demonstrate that any Brønsted−Lowry base that creates a sufficient dose of glycoxide can produce the epi-SL. We then introduce an epi-SL fabrication method that replaces point injection of a base with contactless and uniform illumination of a dissolved photobase. Quantitative mapping of multilayer (3D) films shows that our photobase-made epi-SLs are chemically and structurally uniform and have much lower concentrations of bulk defects compared to the highly inhomogeneous and defect-rich epi-SLs produced by amine point injection. The structural−chemical uniformity and structural perfection of photobase-made epi-SLs make them leading candidates for achieving emergent mini-band charge transport in a self-assembled mesoscale solid.

KEYWORDS: *colloidal quantum dots, superlattice, PbSe, photobase generator, photochemistry, structural characterization, defects*

Photochemical Triggering

QD film

linear diffusion & exchange

PBG $\xrightarrow{h\nu}$ amine $\xrightarrow{EG}$ glycoxide → epi-SL

UV illumination

Epitaxially fused quantum dot (QD) superlattices (epi-SLs) are porous single crystals of epitaxially interconnected colloidal QDs that combine exceptionally high spatial order and strong inter-QD electronic coupling, making them promising materials for studying the emergence of delocalized mini-band transport in self-assembled mesoscale systems.[1−11] PbX (X = Se, S) QD epi-SLs are typically made in two steps. First, a thin-film SL of oleate-capped PbX QDs is self-assembled on the surface of a liquid substrate, usually ethylene glycol (EG).[12−14] Second, the floating oleate-capped SL is converted to an epi-SL by a chemical or thermal treatment that removes oleate from the QD surface, resulting in SL densification and the oriented attachment of adjacent QDs across their {100} facets.[7,9,11,15,16] The epi-SL films are then stamp transferred to solid substrates (the Langmuir−Schaefer process). The most popular chemical trigger for epi-SL formation is 1,2-ethylenediamine (EDA),[7,9,11,16] which has

been proposed to displace oleate from the QD surface *via* Lewis acid−base reactions that form soluble lead oleate complexes such as Pb(EDA)(oleate)$_2$.[9,17,18] However, the absence of EDA and presence of ethylene glycoxide on the surface of epi-SLs fabricated on EG, as well as the absence of leached Pb in the EG, led us to recently conclude that EDA acts instead as a Brønsted−Lowry base that deprotonates EG to form ethylene glycoxide, which then exchanges with oleate on the QD surface.[11] If glycoxide−oleate exchange is dominant, it follows that epi-SL formation should be possible
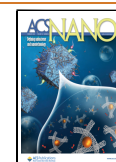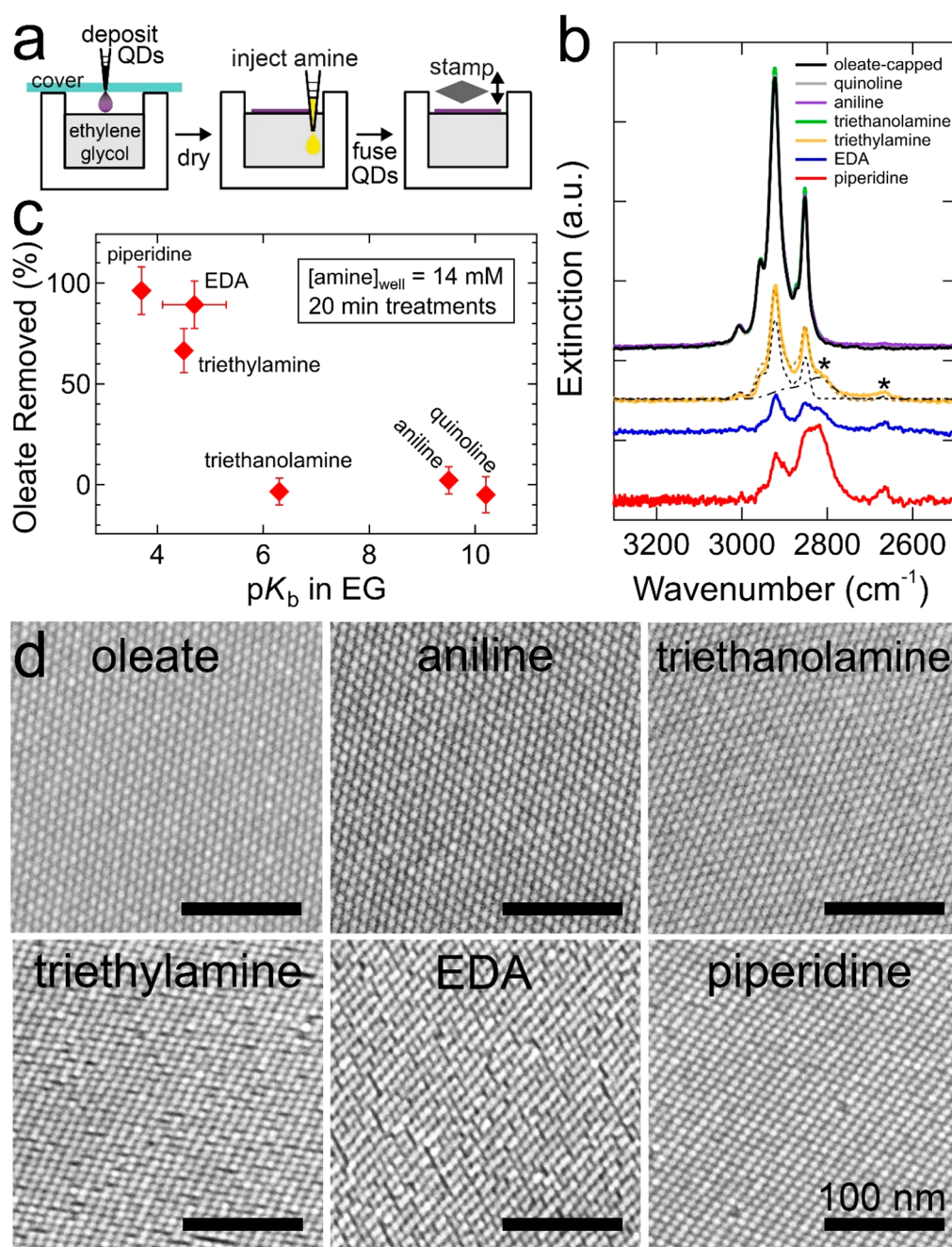
Figure 1. Conversion of oleate-capped PbSe QD SLs to epitaxially fused SLs (epi-SLs) by amine injection. (a) Cartoon of the fabrication process. An amine solution in EG was injected by syringe under the edge of an oleate-capped QD SL film floating on EG in a quartz Petri dish. A portion of the QD film was then stamp transferred onto a double-side-polished silicon substrate. (b) Typical FTIR spectra of an as-made oleate-capped SL (black) and SLs treated by one of six different amines (piperidine, ethylenediamine, triethylamine, triethanolamine, aniline, and quinoline) using a total amine concentration of 14 mM and a 20 min treatment time. The oleate-capped film was aged on the EG surface for 20 min to control for the time spent on EG. All films were 60 ± 10 nm thick. The spectra were baseline corrected, normalized for differences in film coverage of the substrate and QD number density (see Figure S2), and then fit to determine the percent oleate removed (see Figure S3 for fitting details). As an example, the spectrum of the triethylamine-treated film is deconvolved into its oleate-capped component (black dashed line) and glycoxide-capped component (black dash-dotted line, with the two characteristic glycoxide peaks labeled with asterisks). The total fit for this sample is also shown (dashed brown line). All spectra are offset for clarity. See Figure S4 for plots of these spectra over a wider energy range. (c) Plot of the percent oleate removed (as determined from the FTIR spectral fits) *versus* the pK_b for each amine in EG. Experimental pK_b values were taken from the literature,[27−32] while the pK_b of EDA in EG was estimated from Figure S5. Vertical error bars represent the estimated propagated errors. The horizontal error bar on the EDA data point represents the uncertainty in the pK_b value of EDA in EG. EDA = ethylenediamine. (d) Representative plan-view SEM images of the oleate-capped film and the films treated with aniline, triethanolamine, triethylamine, EDA, and piperidine. All scale bars are 100 nm. Quantification of the nearest-neighbor QD−QD distance and local SL symmetry from these images is presented in Figure 3.

using any Brønsted−Lowry base (proton acceptor) that generates a suitable concentration of glycoxide in EG. If this hypothesis could be confirmed, the improved mechanistic understanding would facilitate the rational development of

approaches for fabricating structurally perfect epi-SLs with greatly improved electronic properties.

Here we show that the formation of PbSe QD epi-SLs on the surface of EG is indeed mediated by deprotonated EG (glycoxide) and then use this insight to develop a photochemically triggered, contactless photobase generator (PBG)[19] method to gently make 3D epi-SLs that feature excellent chemical and structural uniformity across their entire areas and much lower concentrations of macroscopic defects compared to epi-SLs made by conventional point injection of an amine into the EG subphase. By dissolving a suitable PBG molecule in the EG, subsequently depositing an oleate-capped SL on the EG surface, and then uniformly illuminating the EG from below with ultraviolet light, we trigger the uniform release of piperidine ($(CH_2)_5NH$) under the QD film to convert the oleate-capped SL into the epi-SL without causing mechanical disturbances that can damage the film or lateral ligand concentration gradients that produce corresponding gradients in ligand coverage, mechanical strain, and QD necking. Our work follows the use of photochemically active ligands[20−23] and dissolved photoacids[24] for direct photopatterning of QD films. In particular, Gao *et al.* recently used a dissolved photoacid generator and a digital light projector to photopattern monolayer (2D) PbS epi-SLs within floating QD monolayers.[24] These authors showed that the oleate coverage and SL structure could be tuned with light dose and photoacid concentration. While our photobase triggering method could be similarly used to pattern epi-SLs, we are mainly interested here in evaluating the ability of unpatterned photochemical triggering to make epi-SLs of unparalleled uniformity and structural quality. With photobase triggering, the structural perfection of an epi-SL is limited by the perfection of the parent oleate-capped SL rather than by inhomogeneities and defects accumulated during the conversion of the oleate-capped SL to the epi-SL. By greatly improving the structural–chemical uniformity and structural quality of epi-SLs and their fidelity with the oleate-capped SLs, this work is an important step toward fabricating QD epi-SLs with sufficient spatial and energetic order to show emergent mini-band transport.

RESULTS AND DISCUSSION

The procedure used in this work to make PbSe QD epi-SLs by conventional amine point injection is shown in Figure 1a. A dispersion of oleate-capped, 6.9 nm diameter PbSe QDs in hexane was pipetted onto the surface of neat ethylene glycol (EG) in a 5 cm diameter cylindrical quartz Petri dish to yield 60 ± 10 nm thick oleate-capped SL films (see Methods). As we recently demonstrated, these oleate-capped SLs adopt a rhombohedrally distorted body-centered cubic superlattice unit cell in which each QD has six nearest neighbors with cofacial {100} facets. This structure enables epitaxial fusion of the {100} facets without the need for large QD rotations and yields a highly ordered epi-SL with a distorted simple cubic unit cell.[11] Then a solution of an amine in EG was injected into the dish underneath the edge of the QD film and, after a prescribed treatment time, the resulting epi-SL film was stamp transferred onto a silicon substrate for characterization by Fourier transform infrared (FTIR) spectroscopy and scanning electron microscopy (SEM). The overall amine concentration in the quartz dish (14 mM) and treatment time (20 min) were chosen to produce EDA-treated epi-SLs with a somewhat high degree of QD epi-fusion and little remaining oleate (∼90% oleate removal relative to the as-made oleate-capped SL films)

at the stamping location (∼0.5 cm toward the center of the film from the injection point). We used a more extreme EDA treatment than in our previous work[11] in order to achieve such high oleate removal and facilitate the evaluation of other amines (*vide infra*), but as a result the EDA-treated films are overly fused and have an excessive degree of necking disorder. FTIR spectra of the EDA-treated films show a large reduction in the intensity of the major oleate peaks (3005, 2924, 2852, 1531, and 1404 cm^{-1}) and the appearance of a broad shoulder at ∼2830 cm^{-1} and a small peak at 2670 cm^{-1} assignable to ethylene glycoxide bound to Pb atoms on PbSe (Figure 1b),[11,25,26] while SEM images indicate a change in structure from the oleate-capped SL to the epi-SL (Figure 1d). Control samples prepared on neat EG without amine injection showed no changes by FTIR or SEM, demonstrating that EG by itself has an insignificant effect on the oleate-capped SLs at these conditions and that EDA is indeed the trigger for oleate removal and epi-SL formation (Figure S1). FTIR spectra of the EDA-treated epi-SLs showed no evidence for adsorbed EDA (Figure 1b), consistent with previous findings.[11] Furthermore, no dissolved Pb has been detected in the EG by inductively coupled plasma mass spectroscopy (ICP-MS).[11] These results are inconsistent with Pb-EDA complex formation, but fully consistent with EDA acting as a Brønsted−Lowry base that deprotonates EG, which then exchanges with oleate on the QD surface (*i.e.*, glycoxide−oleate exchange).

To test the glycoxide−oleate exchange hypothesis, we evaluated a series of amine triggers and found a strong correlation between amine basicity in EG and the extent of both oleate removal and epi-SL conversion. Figure 1c plots the percent oleate removed *versus* the pK_b values of six amines (piperidine, triethylamine, EDA, triethanolamine, aniline, and quinoline). Figure 1d shows representative plan-view SEM images of the films treated in five of these amines. All experiments employed the same amine concentration (14 mM) and treatment time (20 min). The data show that the three strongest bases (lowest pK_b values) removed most of the oleate and triggered epi-SL formation, while the three weakest bases removed no oleate and did not cause epi-fusion of the QDs. Piperidine, the strongest base in the series (pK_b = 3.7), removed the most oleate (96%) and produced moderately fused, high-quality epi-SLs. Triethylamine (pK_b = 4.5) and EDA (pK_b = 4.7) removed 67% and 89% of the oleate, respectively, and produced highly fused epi-SLs. FTIR spectra of these three types of films show the presence of adsorbed glycoxide and the absence of adsorbed amine, consistent with glycoxide−oleate exchange (Figure 1b). In contrast, the weaker bases triethanolamine (pK_b = 6.3), aniline (pK_b = 9.5), and quinoline (pK_b = 10.2) resulted in no oleate removal (Figure 1c), epi-SL conversion (Figure 1d), or glycoxide adsorption (Figure 1b). More extreme treatments with these weaker bases (higher concentrations, longer times) may cause substantial oleate removal and epi-fusion, as was recently reported for aniline treatments of monolayer QD films.[18] We note that factors other than the amine pK_b in EG, such as amine type (primary, secondary, or tertiary), denticity, and size, were not obviously correlated with oleate removal and epi-fusion. We conclude that amines trigger epi-SL conversion indirectly by producing glycoxide that exchanges with oleate on the QD surface.

It should be noted that different exchange mechanisms may be favored depending on the solvent environment. For example, prior work has shown that amines complex with
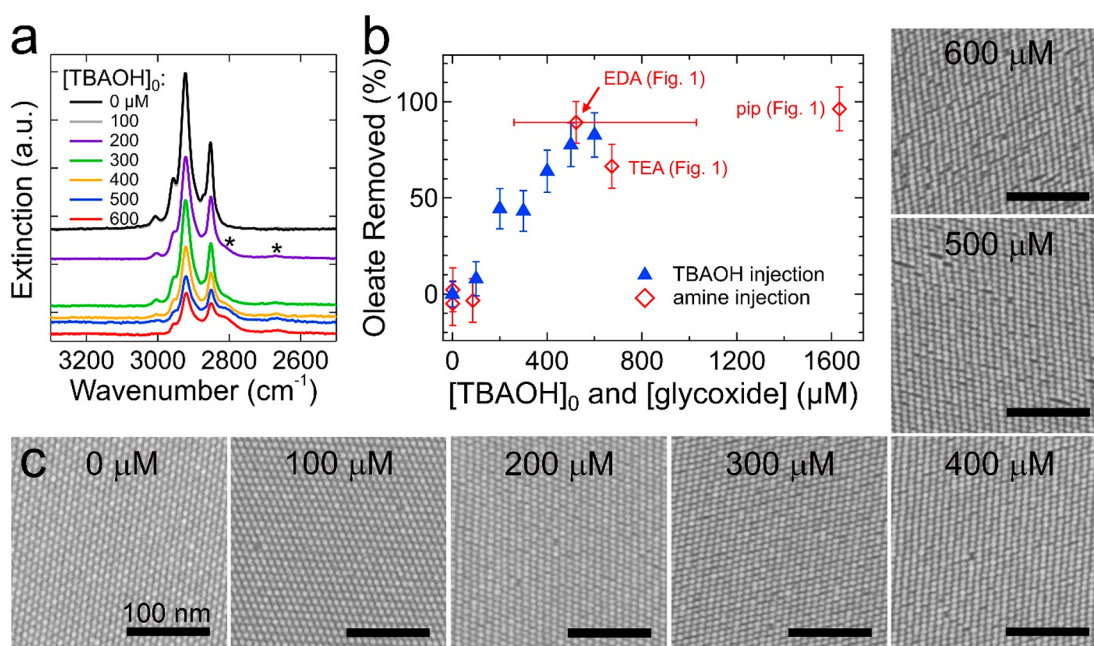
Figure 2. Conversion of oleate-capped SLs to epi-SLs by hydroxide injection. (a) Typical FTIR spectra of an as-made oleate-capped film and films treated with 100−600 μM of TBAOH for 20 min. The spectra were baseline corrected, normalized for differences in film coverage of the substrate and QD number density, and then fit to determine the percent oleate removed, exactly as in Figure 1. All films were 60 ± 10 nm thick. The characteristic shoulder and small low-energy peak of adsorbed glycoxide are labeled with asterisks. See Figure S6 for these spectra plotted over a wider energy range. (b) Plot of the percent oleate removed (as determined from the FTIR spectral fits) *versus* the initial total concentration of TBAOH in the quartz dish (blue triangles). At these low concentrations, TBAOH produces a stoichiometric amount of glycoxide (*i.e.*, $[\text{TBAOH}]_0 = [\text{glycoxide}]$). Overlaid are the data for the films made by amine injection from Figure 1 (red diamonds). The glycoxide concentration for each amine-made film was calculated from the amine concentration and pK_b in EG. The large uncertainty in [glycoxide] produced by EDA is due to the uncertainty in the pK_b value for EDA. Vertical error bars represent the estimated propagated errors. TEA = triethylamine, pip = piperidine, and EDA = ethylenediamine. (c) Representative plan-view SEM images of the hydroxide-made films. Quantification of the nearest-neighbor QD-QD distance and local SL symmetry from these images is presented in Figure 3.

and remove Pb oleate from the surface of PbX QDs in *aprotic* solvents (benzene, toluene).[17] In aprotic solvents, complexation with Pb oleate (the "Lewis mechanism") is perhaps the only mechanism available for oleate removal by amines. However, another mechanism becomes possible in *protic* solvents such as EG: the amines can deprotonate the solvent and the deprotonated solvent anions can directly exchange with oleate, without Pb removal (the "Brønsted mechanism", a focus of much of this paper). We have previously established with direct ICP-MS measurements that the Brønsted mechanism is the dominant mechanism for EDA in EG under the experimental conditions normally used to make epi-SLs.[11] EDA should be a better complexing agent than the other amines in this study because it is a bidentate ligand and one of the strongest Lewis bases among these amines, but EDA shows no Pb removal. Given the chemical similarity of EDA to the other amines studied here, it is very unlikely that the other amines would show appreciable complexation and stripping of Pb when EDA shows none. Nevertheless, it is possible that both the Lewis and Brønsted mechanisms may be simultaneously active and important for some protic solvent/amine pairs, and it may be the case that some amines remove some amount of Pb even in EG. Previous work has indeed suggested that amines remove Pb from PbX QDs floating on EG,[18] but the evidence for Pb removal (subtle changes in UV−vis spectra, TEM size histograms, and energy dispersive spectra after treatment with *n*-butylamine) was indirect and inconclusive. Direct measurements of Pb removal (*e.g.*, by ICP-MS)

should be performed to determine the relative importance of the Lewis and Brønsted mechanisms for a greater number of amines. Based on ref 11 and the current work, we expect that *n*-butylamine (pK_b = 3.4 in water and probably ∼4.0 in EG, similar to EDA and piperidine) acts similarly to EDA and removes oleate by glycoxide−oleate exchange rather than complexation with Pb oleate.

We next reasoned that if glycoxide−oleate exchange is indeed the chemical mechanism that triggers epi-SL formation, then replacing the amine with a nonamine base that generates sufficient glycoxide should also produce the epi-SL. The simplest such base is hydroxide ion (OH⁻), which deprotonates EG to form water and glycoxide:

$$\text{OH}^- + \text{HO(CH}_2)_2\text{OH} \rightleftharpoons \text{H}_2\text{O} + \text{HO(CH}_2)_2\text{O}^-$$
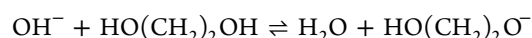
Figure 2 presents FTIR spectra and SEM images of QD films treated with various concentrations of tetrabutylammonium hydroxide (TBAOH), a hydroxide salt selected because it is reasonably soluble in EG and delivers a cation with no complicating acid/base properties or affinity for the QD surface. We find that the hydroxide-treated and amine-treated films have nearly identical FTIR spectra and SEM images for the same effective glycoxide concentration. As with the amine treatments, the FTIR spectra of films treated with hydroxide show loss of oleate, the presence of adsorbed glycoxide, and no evidence for adsorption of the treatment molecule itself (Figure 2a). The degree of both oleate removal and epi-fusion increased with increasing initial TBAOH concentration

([TBAOH]$_0$) from 0 to 600 μM (Figure 2b,c). Oleate removal shows a sigmoidal dependence on [TBAOH]$_0$, increasing rapidly from ~8% at [TBAOH]$_0$ = 100 μM and then slowing to ~83% at [TBAOH]$_0$ = 600 μM. We note that TBAOH is expected to quantitatively deprotonate EG, such that [glycoxide] = [TBAOH]$_0$. Recasting [TBAOH]$_0$ in terms of [glycoxide] permits a direct comparison with the oleate removed by the amines, for which [glycoxide] is readily calculated from the amine concentration and pK_b value in EG. The data are in good agreement (Figure 2b), suggesting that the amount of oleate removed from the QD films is largely determined by the glycoxide dose generated from the injected base (either TBAOH or amine). Meanwhile, the SEM image series shows that the oleate-capped SL converts to the epi-SL when [TBAOH]$_0$ $\geq$ 200 μM (Figure 2c). Epi-SLs made at intermediate [TBAOH]$_0$ appear to have the best structural order, while the QDs are somewhat overfused and the films more defective at the higher TBAOH concentrations ($\geq$500 μM). These results demonstrate that amines are not needed for epi-SL formation and suggest that any base that produces a sufficient amount of glycoxide can trigger the epi-SL transformation on EG. In general, a base added to a protic solvent such as EG is expected to produce some concentration of deprotonated solvent anions that can act as X-type ligands to replace oleate. Indeed, it is likely that many anions other than glycoxide (e.g., thiocyanate, halides, carboxylates) can exchange with oleate to produce high-quality epi-SLs. The main requirement seems to be that the supplied anion displaces oleate while the cation forms an oleate salt that is sufficiently soluble in EG. It is also possible for Brønsted–Lowry acids (e.g., carboxylic acids, alkylammonium iodides) to protonate and remove oleate as oleic acid and replace it with the attendant anion (carboxylate, iodide).[33,34] Thus, there are both basic and acidic routes to oleate ligand exchange and epi-SL formation.

We quantitatively analyzed SEM images of the amine- and hydroxide-treated films to extract three metrics that characterize the degree of oleate- to epi-SL conversion: the in-plane inter-QD distance, QD number density (QDs/nm^2), and SL symmetry. Details about the image analysis are presented in Figure S7. Figure 3 shows d, the center-to-center distance between neighboring QDs along the [100] superlattice direction (blue markers), and the squareness parameter Ψ_4,[35–37] which provides a local measure of the degree of 4-fold symmetry of the SL (red markers). We observe a sudden change in both parameters at a threshold glycoxide concentration of ~200 μM. The average inter-QD distance decreases from 8.3–8.6 nm for [glycoxide] $\leq$ 100 μM to 6.7–7.3 nm for [glycoxide] $\geq$ 200 μM, with the EDA and 600 μM TBAOH treatments resulting in the smallest average distances (6.7 and 6.8 nm, respectively, just 1–2 Å larger than the diameter of these truncated cuboctahedral QDs in the $\langle 100 \rangle$ directions). The inter-QD distance also decreases slightly from 7.3 to 6.8 nm with increasing TBAOH concentration from 200 to 600 μM. Meanwhile, Ψ_4 jumps from 0.29–0.39 for [glycoxide] $\leq$ 100 μM to 0.51–0.56 for [glycoxide] $\geq$ 200 μM. The step-like change in these two parameters indicates that the epi-SL phase transition occurs abruptly over a narrow range of [glycoxide]. Sufficient oleate exchange with glycoxide enables strong inter-QD interactions that lead to a sudden change in local SL symmetry and concurrent densification of the SL. As the interdot distance shrinks, the QDs "click" together, forming a rigid distorted simple cubic lattice with the
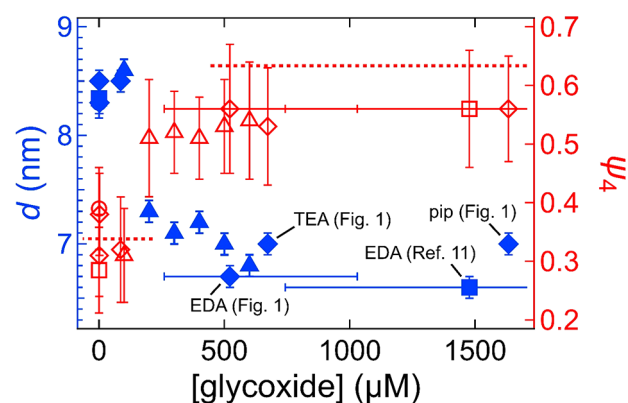

Figure 3. Lateral inter-QD distance (d, left axis, blue markers) and superlattice squareness parameter (Ψ_4, right axis, red markers) for the amine- and hydroxide-treated films. Diamonds and triangles are the amine-treated films and TBAOH-treated films, respectively. Circles are an as-made oleate-capped film aged for 20 min on EG. Squares are the oleate-capped and EDA-treated films reported in ref 11. The QDs used in ref 11 had an idealized spherical diameter of 6.5 nm, compared to 6.9 nm in the current work. Horizontal red dashed lines are calculated Ψ_4 values for the unit cells of the oleate-capped SL and epi-SL in ref 11. Vertical error bars are standard deviations. Horizontal error bars represent the uncertainty in [glycoxide] for EDA. TEA = triethylamine, pip = piperidine, and EDA = ethylenediamine. See Figure S8 for comparative plots of oleate removal, inter-QD distance, area per QD, and density increase for these types of samples.

QDs fused along their {100} facets.[11] Additional fusion leads to only a small additional decrease in the inter-QD distance as the necks thicken and shorten.

Since SEM measures only the outer surface of the QD films, the use of plan-view SEM images to infer bulk film structure must be experimentally validated. To do this, we imaged the top and bottom surfaces of several representative epi-SLs and found that the two surfaces have effectively identical structures, implying uniform ligand exchange and epi-fusion across the thickness of each film (Figure S9). We therefore believe that the surface and bulk of these films are very similar, and our plan-view SEM images faithfully represent the bulk structure of the epi-SLs.

Equipped with the knowledge that epi-SL conversion on EG is mediated by deprotonated solvent (glycoxide), we hypothesized that the uniformity and structural order of the epi-SLs could be improved by changing the triggering method from point injection of a base to uniform illumination of a dissolved photobase.[19] Figure 4a illustrates our photobase method and some of its anticipated advantages over point injection. In the photobase approach, an oleate-capped SL is assembled on EG that contains a predissolved photobase generator molecule. The PBG itself is a very weak base (high pK_b) that does not cause QD fusion or otherwise affect the oleate-capped SL. However, when illuminated with light of the proper wavelength, the PBG releases a stronger base (lower pK_b) that produces sufficient glycoxide to trigger epi-SL conversion. The PBG used here is (E)-1-piperidino-3-(2-hydroxyphenyl)-2-propen-1-one (code named WPBG-027), which undergoes photochemical cleavage to release piperidine (pK_b = 3.7 in EG) when illuminated with UV light (Figure 4b). Structural and optical characterization of this PBG are provided in Figure S10. Photobase illumination promises to yield films with better structural–chemical uniformity, less
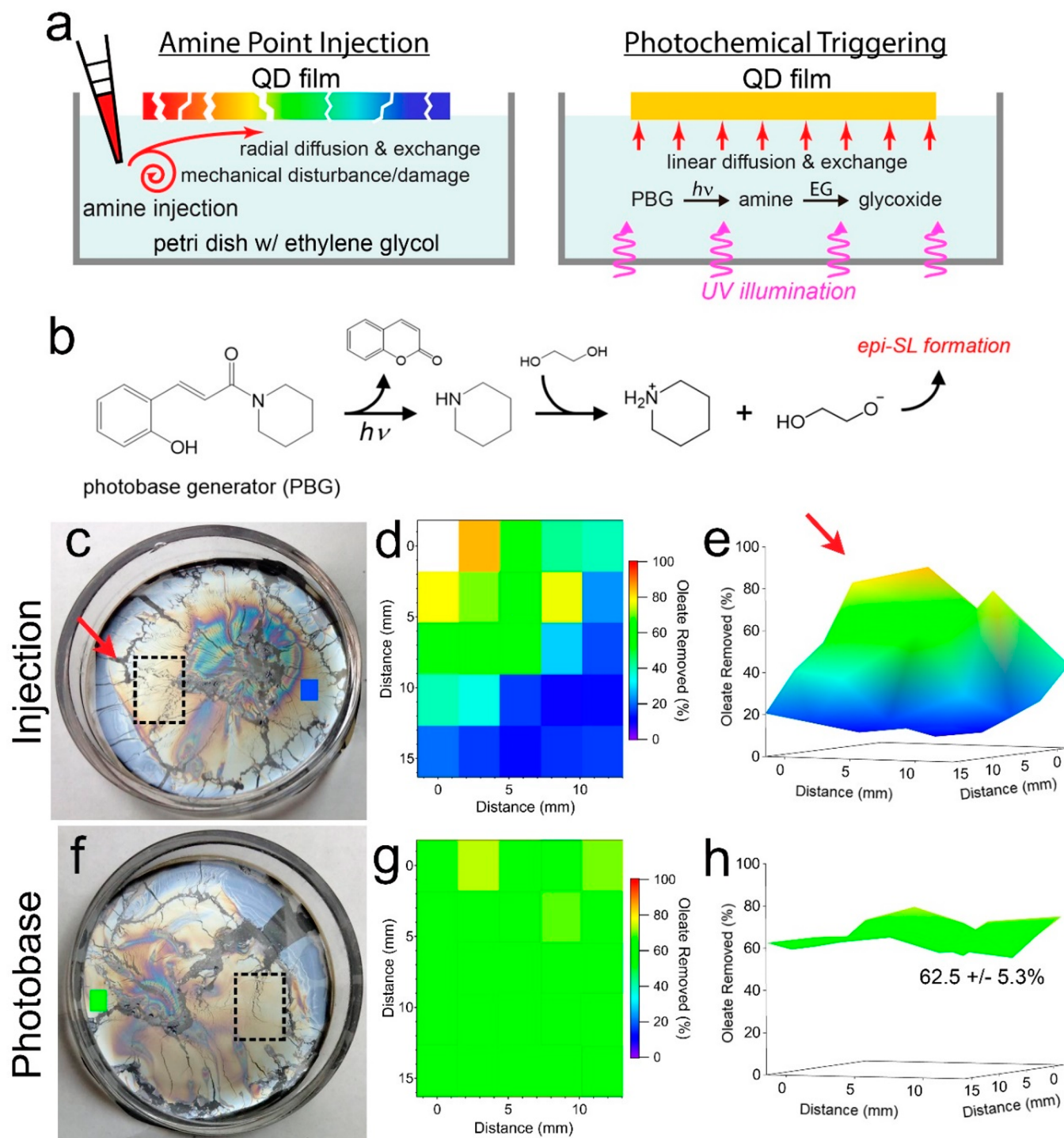
Figure 4. Photochemically triggered epi-SL conversion and uniformity of the resulting films. (a) Schematic depictions of the conventional point injection method (left) compared to our photobase method of making epi-SLs (right). Contactless illumination of a photobase generator (PBG) molecule predissolved in the EG yields a laterally uniform glycoxide concentration and glycoxide−oleate ligand exchange while avoiding the damaging mechanical disturbances of point injection. The color of the QD films denotes the degree of local oleate removal. (b) Proposed reaction cascade for photochemically triggered epi-SL conversion. Photodissociation of the PBG WPBG-027 produces piperidine, which deprotonates EG to form glycoxide, triggering glycoxide−oleate exchange and conversion of the oleate-capped SL to the epi-SL. (c−e) Results for piperidine point injection. The photograph in (c) shows a floating oleate-capped SL film prior to piperidine injection. The red arrow, dashed rectangle, and small blue rectangle denote the location of piperidine injection, the area mapped by FTIR, and an additional point on the far side of the film measured by FTIR, respectively. The diameter of the Petri dish is 5 cm. (d) 2D map (5 × 5 array) of the percent oleate removed from the film as determined by FTIR measurements of the stamp-transferred film. The mapped area is indicated by the dashed rectangle in (c). The injection point is to the left of the upper left corner of the map. One data point is missing from the map due to delamination of the QD film at that location. All quantification corrections were applied as per Figure 1. As expected, there is a marked oleate concentration gradient in the injection-made film. The blue color of the rectangle on the far side of the film in (c) is consistent with this gradient. Film treatment conditions: 0.5 mL of 11 mM piperidine in EG slowly injected into the 5 mL EG

Figure 4. continued

subphase, exchanged for 1 h (1 mM piperidine overall, equivalent to 360 μM glycoxide). (e) 3D view of the map. The red arrow denotes the injection point. (f–h) Results for photobase illumination. (f) Photograph of the floating film before illumination. The dashed rectangle and small green rectangle denote the area mapped by FTIR and an additional point on the far side of the film measured by FTIR, respectively. (g) 2D map (5 × 5 array) of the percent oleate removed, as per (d). The percent oleate removed is constant within experimental error. The green color of the rectangle on the far side of the film in (f) shows that the entire film has uniform ligand exchange. Film treatment conditions: 1 mM PBG in the subphase, 1 h illumination with 254 nm light @ 1.5 mW cm^{-2} followed by 4 h of additional exchange in the dark. (h) 3D view of the map. Oleate removal in the mapped region is 62.5 $\pm$ 5.3%. Both films are 60 $\pm$ 10 nm thick. See Figure S17 for a photograph of the experimental setup for photochemically triggered epi-SL conversion.

mechanical damage, and better control of the glycoxide dose than conventional point injection. In contrast to point injection, which produces a radial concentration gradient of glycoxide under the QD film that results in laterally nonuniform degrees of ligand exchange and epi-fusion, illumination of a PBG dissolved in the subphase should produce a uniform glycoxide concentration in the plane of the film, enabling laterally uniform ligand exchange and QD fusion across the entire epi-SL. Furthermore, whereas point injection causes vibration, surface waves, convective liquid currents, vortices, and other mechanical disturbances that can damage the delicate floating QD film, the photobase method is contactless and gentle and avoids mechanical damage. Finally, photobase triggering provides a convenient way to control the glycoxide dose (concentration–time profile) by adjusting the illumination intensity and time, which may allow for the fabrication of more perfect epi-SLs by fine-tuning the kinetics of ligand exchange and epi-fusion. Here we focus on the first two advantages (better film uniformity and reduced mechanical damage), leaving an investigation of the importance of improved glycoxide dose control for future work.

It is reasonable to ask if similar ends could be achieved more easily by simply dissolving a conventional base (*e.g.*, an amine or hydroxide) in the EG before depositing the QD suspension on the EG surface. This approach might also yield laterally uniform, contactless ligand exchange while avoiding the added complexity of photochemical triggering. However, casting the QD dispersion onto EG that already contains a significant amount of base (and thus glycoxide) results in poor-quality, nearly amorphous films because self-assembly and ligand exchange occur simultaneously rather than sequentially (Figure S11). The glycoxide generated by the base begins to strip oleate from the QDs as soon as the two solutions make contact, ruining SL formation. Adding base to the EG prior to casting the QD film is not a viable strategy for making epi-SLs. To make a high-quality epi-SL, it is essential to first assemble a high-quality oleate-capped SL and then trigger epi-SL conversion with base addition. Self-assembly and ligand exchange must be separated in time to make good films.

FTIR and SEM mapping were used to compare the lateral chemical and structural uniformity of films made by amine point injection *versus* photobase illumination (Figure 4c–h and Figure S12). Figure 4c shows a photograph of a floating oleate-capped SL film prior to piperidine injection. A solution of piperidine in EG was carefully injected into the subphase near the edge of the film (red arrow) and allowed to diffuse and exchange with the film for 1 h, at which time the film was stamped onto a silicon substrate for analysis (see Methods). A 1.5 × 1.2 cm region of the film close to the injection point was mapped by FTIR spectroscopy (5 × 5 array, dashed rectangle in Figure 4c). The resulting map of oleate removal shows a pronounced radial gradient, as expected, with oleate loss

decreasing from ∼85% closest to the injection point to only ∼15% farthest from the injection point (Figure 4d,e). Our setup made it inconvenient to map the entire QD film, but we did measure one additional point at the far side of the floating film (blue rectangle in Figure 4c) and found an oleate loss of 17%, which is consistent with a fairly steep ligand exchange gradient around the injection point and relatively little oleate removal (10–20%) across most of the film. Replotting these data as a function of distance from the injection point shows that oleate removal decreases rapidly with distance and falls below 20% at ∼1.5 cm from the injection location (Figure S13). SEM images collected at the 25 FTIR spots were used to make corresponding maps of inter-QD distance, film densification, and area per QD. These three parameters exhibit radial gradients similar to that of oleate removal (Figure S12). Visual inspection of the SEM images shows that the degree of epi-fusion decreases with radial distance and that no epi-fusion occurs beyond ∼1.7 cm from the injection point. We also found a strong inverse dependence of the inter-QD distance on oleate removal and an apparent threshold of >25% oleate removal for conversion of the oleate-capped SL to the epi-SL (Figure S14). Overall, it is clear that point injection produces highly inhomogeneous films with strong lateral gradients in ligand coverage, inter-QD distance, and epi-fusion.

In contrast to films made by piperidine injection, films made by photobase illumination are very homogeneous, with uniform oleate removal, inter-QD distance, and epi-fusion across the entire film surface. Figure 4f shows a photograph of a floating oleate-capped SL film prior to illumination. The EG subphase contained 1 mM of the PBG. The film was then illuminated from below with 254 nm light from a mercury lamp (1.5 mW cm^{-2}) for 1 h and exchanged for another 4 h in the dark before being stamped onto silicon. The map of oleate removal shows a uniform value of 62.5 $\pm$ 5.3% (Figure 4g,h). The point on the far side of the film (green rectangle in Figure 4f) had an oleate loss of 57%, demonstrating uniformity across the entire film. The maps of inter-QD distance, film densification, and area per QD are similarly uniform, with values of 7.25 $\pm$ 0.11 nm, 13.8 $\pm$ 2.7%, and 67 $\pm$ 2 nm^2/QD, respectively (Figure S12). These narrow distributions reflect the inherent lateral uniformity of photobase-triggered epi-SL conversion. FTIR spectra of the photobase-made films were indistinguishable from spectra of films made by piperidine injection, with both showing adsorbed glycoxide but no adsorbed piperidine, which is again consistent with glycoxide–oleate exchange (Figure S15).

Control experiments confirmed that photochemically triggered epi-SL conversion requires both the PBG and UV illumination. Films illuminated in the absence of PBG showed minimal oleate loss (<10%) and no epi-fusion (Figure S16). Films exposed to PBG without UV light had somewhat higher oleate removal (∼15%) but no epi-fusion. Since the UV lamp

**Table 1. Statistical Comparison of Injection-Made and Photobase-Made epi-SLs**

	parameter	injection-made epi-SLs	photobase-made epi-SLs
from FTIR spectra	oleate removed	59 ± 9%	54 ± 9%
from high-mag images	densification	15 ± 3%	13 ± 4%
	d (FFT)	7.1 ± 0.1 nm	7.2 ± 0.1 nm
	d (direct)	7.0 ± 0.4 nm	7.1 ± 0.3 nm
	Ψ_4	0.552 ± 0.089	0.565 ± 0.085
	nanotear density	29 ± 12 μm^{-2}	6 ± 6 μm^{-2}
	chain split density	68 ± 23 μm^{-2}	4 ± 4 μm^{-2}
from low-mag images	crack density[a]	4.9 ± 1.2 μm^{-2}	0.79 ± 0.21 μm^{-2}
	crack area[a]	2.4 ± 0.33% of film	0.63 ± 0.22% of film

[a]Includes all visible intraflake extended defects (larger nanotears and cracks/voids). Neglects interflake cracks.

also slightly warms the samples (to 37−38 °C), we ran additional control experiments in which floating films were aged on a hot plate at 38 °C without UV illumination. Samples heated without PBG had <10% oleate loss and no epi-fusion, while samples heated with PBG showed ~22% oleate loss, but again the epi-SL did not form. Only PBG together with UV illumination resulted in major oleate loss (~65%) and formation of the epi-SL. These control experiments demonstrate that epi-SL conversion is caused by the proposed photochemistry rather than an alternative mechanism such as dark aging of the QD film by EG or the PBG, film heating, or direct excitation of the film by UV light.

Comparison of the d and Ψ_4 values of these samples reveals that contact with EG itself causes moderate densification and structural evolution of the floating QD films. For all of the control samples (5 h on EG), d = 7.7−8.0 nm and Ψ_4 = 0.43−0.47, compared to d = 8.6 nm and Ψ_4 = 0.29 for the oleate-capped SLs and d = 7.2 nm and Ψ_4 = 0.57 for the epi-SLs made by photobase illumination (Figure S16). We speculate that wetting of the films by EG increases oleate interdigitation, compaction, and/or diffusion on the QD surface, resulting in the observed density and squareness increase despite the small amount of oleate removed from these samples. In fact, even films aged for only 20 min on pure EG—for which oleate loss was negligible—showed significant changes in d and Ψ_4 (d = 8.3 nm and Ψ_4 = 0.39, Figure S16).

SEM imaging was used to compare the morphologies and structural defect concentrations of the photobase-made and injection-made films. Films made as per Figure 4 were imaged in many different locations at both "high" and "low" magnification. The photobase-made films, which are laterally uniform (Figure 4), were imaged at randomly selected spots across their entire surfaces, while the injection-made films were imaged at randomly selected spots within the small region of each film that had values of oleate removal, inter-QD spacing, and Ψ_4 equivalent to those of the photobase-made films (see Table 1). Figure 5 presents representative images of both types of films. The high-magnification images (Figure 5a and c) show that the injection-made films have a much higher concentration of nanoscale extended defects. Some of these defects are relatively large nanoscale tears/rips in the films (individual examples of which are highlighted with the red ovals in Figure 5). For the purposes of this paper, we refer to such tears as "nanotears" if they have a short dimension of 5−25 nm. In addition to nanotears, the injection-made films also contain a large number of thinner (<5 nm) parallel tears that cut across the QD chains of the $(01\bar{1})_{SL}$ superlattice grains, splitting the QD chains into shorter segments (e.g., see blue oval in Figure 5a). These defects are rows of missing necks
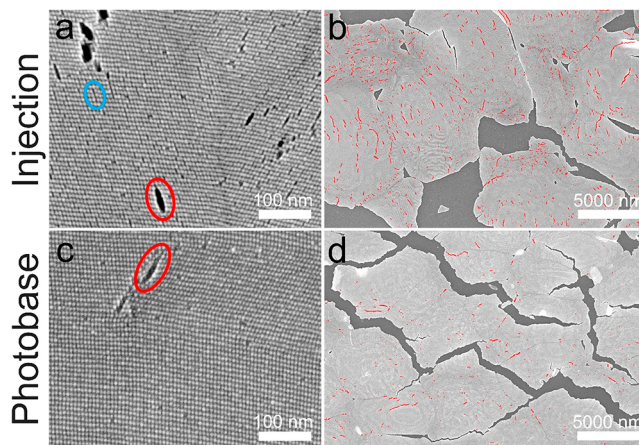
Figure 5. Morphology comparison of photobase-made and injection-made epi-SLs. (a) Representative high-magnification image of an epi-SL film made by piperidine injection, showing a high density of nanoscale tears (e.g., red oval) and $[100]_{SL}$ chain splits (e.g., blue oval). The scale bar is 100 nm. (b) Representative low-magnification image of an injection-made film, showing a high density of intraflake cracks (shaded red). Interflake cracks are unshaded. The scale bar is 5000 nm. (c, d) Corresponding representative images of photobase-made epi-SLs, showing the absence of chain splits and significantly lower density of nanotears and cracks (shaded red in d). See Table 1 for a quantitative statistical comparison of the two film types. Film fabrication conditions as per Figure 4.

between QDs. We classify these defects as "chain splits" if they are at least three QDs long. Chain splits are ubiquitous in the injection-made films but rare in the photobase-made films. We quantitatively analyzed over two dozen images to determine the typical concentration of nanotears and chain splits in the two types of films. We find a nanotear density of 29 ± 12 μm^{-2} in the injection-made films versus 6 ± 6 μm^{-2} in the photobase-made films, while the density of chain splits is 68 ± 23 and 4 ± 4 μm^{-2}, respectively. The photobase-made films have much lower densities of nanotears and chain splits. Table 1 summarizes these statistics. We also found high concentrations of nanotears and chain splits in injection-made films that had more oleate (only 40−50% oleate removal) and a larger inter-QD distance (7.2−7.4 nm) than the photobase-made films, demonstrating that high defect densities are a robust characteristic of the injection-made films and not the result of excessive QD fusion or small sample-to-sample differences in oleate content or inter-QD distance (Figure S18).

While the high-magnification images show the small extended defects, the low-magnification images provide information about the morphology and distribution of the bigger defects, particularly cracks within individual flakes in a film (intraflake cracks) and between adjacent flakes in a film (interflake cracks). Representative low-mag images (Figure 5b and d) demonstrate that the photobase-made films have fewer and smaller intraflake cracks than the injection-made films. Note that in these low-mag images the chain splits and smaller nanotears are not visible and many of the closely spaced nanotears appear as single continuous cracks, so the cracks are undercounted. By analyzing five images of each film type, we find an intraflake crack density of $4.9 \pm 1.2 \; \mu m^{-2}$ in the injection-made films and only $0.79 \pm 0.21 \; \mu m^{-2}$ in the photobase-made films (Table 1, Figure S19, and Table S1). These cracks account for $2.4 \pm 0.33\%$ and $0.63 \pm 0.22\%$ of the total area of the flakes in the injection-made and photobase-made films, respectively. The intraflake cracks are shaded red in Figure 5b and d. These shaded images emphasize that the injection-made films are riddled with cracks, many of which are clustered together in parts of the films, while the photobase-made films have significantly fewer cracks.

There are several possible explanations for the lower concentration of chain splits, nanotears, and intraflake cracks in the photobase-made films. First, since photochemical triggering avoids the mechanical disturbances caused by point injection (*e.g.*, vibrations and bulk liquid flow), the photobase-made films may suffer less mechanical damage. Second, differences in ligand exchange dynamics may result in fewer defects in the photobase-made films. In particular, it is likely that the laterally uniform and slower ligand exchange enabled by photobase illumination produces less mechanical stress in the film compared to the radial concentration gradient and propagating reaction fronts inherent to point injection. A third possibility is that the photobase-made epi-SLs are mechanically stronger and therefore less damaged when stamped from the EG surface to a solid substrate. While it is clear that photobase-made films have far fewer extended defects than do the injection-made films, we cannot determine from our current data exactly why this is the case.

Both the photobase-made and injection-made films have extensive interflake cracking (the unshaded cracks in Figures 5b,d and S19). In general, the photobase-made epi-SLs are more continuous and their flakes are better interconnected, but the difference is small. Image quantification shows that the photobase-made films cover 91.4% of the substrate, compared with only 82.5% for the injection-made films (Table S1). Some, and perhaps most, of the interflake cracks are created when the films are stamped from EG onto the Si wafer, which is itself a very violent process and probably the most intractable limitation on epi-SL film quality for current implementations of the Langmuir–Schaefer approach. Another major source of interflake cracks is volume loss and film contraction during ligand exchange and epi-fusion prior to stamping. The extent of inter- and intra-flake crack creation from epi-SL conversion depends on a number of complex and poorly understood factors, including the size, interconnectedness, and structural perfection of the grains of the parent oleate-capped SL and the dynamics of ligand exchange and epi-fusion. As mentioned above, photochemical triggering may offer a convenient way to spatiotemporally tune the glycoxide dose and control the exchange kinetics to reduce the concentration of cracks and tears arising from volume loss. However, it is ultimately the structural perfection of the parent oleate-capped SL that determines the concentration of extended defects in the epi-SLs. Cracks tend to form at weak spots in these films, such as along SL grain boundaries. Therefore, the most promising way to make less defective epi-SLs is to increase the grain size and improve the intragrain spatial order of the oleate-capped SLs, which is the focus of ongoing work in our laboratories.

CONCLUSION

This work shows that conversion of oleate-capped PbSe quantum dot superlattices into epitaxially fused superlattices by the standard method of amine injection into an ethylene glycol subphase is mediated by glycoxide–oleate ligand exchange. In this mechanism, the amine deprotonates ethylene glycol to form glycoxide, which then replaces oleate on the QD surface, decreasing the inter-QD spacing and triggering fusion across the {100} facets to form the epi-SL. The percent oleate removal, inter-QD distance, and degree of epi-fusion are strongly correlated with amine pK_b in ethylene glycol, suggesting that the glycoxide concentration (dose) drives epi-SL formation. Essentially identical results were obtained by replacing the amines with tetrabutylammonium hydroxide. Quantitative agreement between the amine- and hydroxide-treated films in terms of oleate removed, inter-QD spacing, and Ψ_4 as a function of [glycoxide] establishes that the glycoxide dose is the single most important factor governing epi-SL conversion. We found that the epi-SL phase transition occurs abruptly at a threshold glycoxide concentration ($\sim$200 μM at these conditions).

The insight that epi-SL conversion is mediated by a Brønsted–Lowry acid–base reaction between the injected base (amine or hydroxide) and ethylene glycol was then leveraged to propose photobase triggering as a fundamentally better way to make epi-SLs. FTIR and SEM mapping showed that bottom UV illumination of a piperidine-producing photobase generator dissolved in the ethylene glycol subphase resulted in epi-SLs with excellent chemical and structural uniformity compared to the highly inhomogeneous epi-SLs made by piperidine point injection, the latter of which exhibited strong lateral gradients in oleate coverage, inter-QD distance, and epi-fusion. Photochemically made films not only are more uniform but also contain much lower concentrations of small extended structural defects such as tears and cracks, probably in part because photobase illumination is contactless and avoids the damaging mechanical disturbances caused by point injection. Statistical analysis of SEM images showed that photobase-made films have five times fewer nanotears, 17 times fewer chain splits, and six times fewer intraflake cracks compared to injection-made films with equivalent values of oleate content, inter-QD distance, and Ψ_4. The structural–chemical uniformity and structural perfection of these photobase-made epi-SL films make them leading candidates for achieving emergent mini-band charge transport in a self-assembled mesoscale solid. Our photochemical-triggering approach also provides a way to scale up epi-SL fabrication and implement (low-resolution) photopatterning for optoelectronic devices.

METHODS

Materials. All chemicals were used as received unless otherwise noted. Lead oxide (PbO, 99.999%) and selenium shot (99.999%) were purchased from Alfa Aesar. Oleic acid (OA, technical grade, 90%), diphenylphosphine (DPP, 98%), 1-octadecene (ODE, 90%),

anhydrous ethylene glycol (EG, 99.8%), anhydrous acetonitrile (99.99%), anhydrous hexanes (99%), anhydrous toluene (99.8%), 3-mercaptopropyltrimethoxysilane (3-MPTMS, 95%), aniline (≥95%), triethanolamine (TEA, GC, ≥99.0%), tetrabutylammonium hydroxide 30-hydrate (TBAOH, 99.0%), and dimethyl sulfoxide-d_6 (DMSO-d_6, anhydrous, 99.9 atom % D) were purchased from Sigma-Aldrich. Anhydrous 1,2-ethylenediamine (EDA, >98.0%) was purchased from TCI. Piperidine (99%) was purchased from Spectrum Chemical. Quinoline (99%), triethylamine (99%), and coumarin (99%) were purchased from Fisher Scientific. (E)-1-Piperidino-3-(2-hydroxyphenyl)-2-propen-1-one (WPBG-027) was purchased from Fujifilm. Trioctylphosphine (TOP, technical grade, >90%) was acquired from Sigma-Aldrich and mixed with selenium shot for 24 h to form a 1 M TOP-Se stock solution. Nitric acid (TraceMetal grade, Fisher Scientific) was distilled twice before use, and 18.2 MΩ water (Milli-Q Gradient) was used for substrate cleaning.

Quantum Dot Synthesis. PbSe QDs were synthesized and purified using standard air-free techniques. PbO (1.50 g), OA (5.00 g), and ODE (10.00 g) were mixed and degassed in a three-neck round-bottom flask at room temperature. The mixture was then heated at 120 °C under vacuum to form lead oleate (Pb(OA)$_2$) and dry the solution. After 1.5 h, the Pb(OA)$_2$ solution was heated to 180 °C under argon flow, and 9.5 mL of a 1 M solution of TOP-Se containing 200 μL of DPP was rapidly injected into this hot solution. An immediate darkening of the solution was observed, and the QDs were grown for 105 s at ~160 °C. The reaction was quenched with a liquid nitrogen bath and injection of 10 mL of anhydrous toluene. The QDs were purified in an N$_2$-filled glovebox (<0.5 ppm of O$_2$) by adding 20 mL of acetonitrile to the reaction solution, collecting the QDs by centrifugation, performing 7−9 cycles of redispersion/precipitation using acetonitrile/toluene (20 mL/5 mL), and then drying and storing the QDs as a powder in the glovebox.

Superlattice Fabrication by Amine or TBAOH Injection. SL fabrication was performed at room temperature in a N$_2$-filled glovebox with <0.5 ppm of O$_2$. Oleate-capped PbSe QD superlattices were prepared by carefully drop-casting 90 μL of a 10 mg/mL solution of PbSe QDs dispersed in hexanes onto 5 mL of ethylene glycol in a quartz Petri dish (5 cm diameter). The dish was previously cleaned by soaking overnight in a base bath (1.5 M KOH in isopropanol) and then thoroughly rinsed in deionized water and dried in an oven at 110 °C. After depositing the QD solution, the dish was immediately covered by a glass plate with an O-ring glued to its underside to improve the vapor seal. The hexane was allowed to slowly evaporate over ~10 min, resulting in a smooth, dry oleate-capped QD film floating on the EG surface. The cover was then removed and the desired amount of the chemical trigger (amine or TBAOH solution in EG) was slowly (5−10 s) injected into the EG under an edge of the film. As the chemical trigger spread throughout the dish, the film visibly darkened, indicating film densification and epi-SL formation. After an appropriate treatment time, an area of the darkened SL film ~0.5 cm from the injection point was transferred to a silicon substrate by manual stamping using a vacuum wand. All substrates were cleaned by 15 min of sonication each in acetone, water, and isopropanol, dried under flowing air, soaked in a 100 mM solution of 3-MPTMS in toluene for 1 h inside the glovebox to functionalize the surface for improved QD adhesion, and then rinsed with neat toluene and dried under flowing N$_2$. The stamped film was rinsed vigorously with neat acetonitrile and dried under flowing N$_2$. This procedure results in epi-SLs consisting of roughly rectangular grains with an average lateral size of 1.2 × 0.4 μm as measured by SEM.

Superlattice Fabrication by Photobase Triggering. SL fabrication was again performed in a N$_2$-filled glovebox with <0.5 ppm of O$_2$. The Petri dish was filled with 5 mL of 1 mM PBG in EG and set on a stand ~1.5 cm above a UV lamp (UVGL-58, UVP). The oleate-capped QD film was then made on the EG surface as described above. The UV lamp was then switched on to illuminate the entire Petri dish (254 nm, ~1.5 mW/cm^2 at the film position) for 1 h (during which time the films were gradually heated by the UV lamp to 37−38 °C), after which the film sat on the EG for an additional 4 h in the dark before the desired region was stamped onto a silicon

substrate, rinsed thoroughly with neat acetonitrile, and dried under flowing N$_2$.

Characterization. FTIR extinction spectra of QD films deposited on 500 μm thick, double-side-polished, intrinsic float zone Si substrates (University Wafer) were acquired in dry air at room temperature on a Nicolet 6700 FTIR spectrometer using an XT-KBr beamsplitter and a TE-cooled DLaTGS detector. The substrate was aligned perpendicular to the beam (transmission mode). Spectra were collected at a resolution of 4 cm^{-1} using 64 scans acquired at 0.26 scans/s. A clean Si substrate was used as the background. The spectra were baseline corrected across the C−H stretching region to enable accurate determination of oleate removal by fitting each baseline using a spline function in Igor Pro and then subtracting the baseline from the raw spectrum to yield the corrected spectrum. The spline function was tailored to each spectrum in order to produce a flat baseline in the region of interest. Spline points were selected in featureless regions of the spectra (~5000−4000 and ~2600−2000 cm^{-1}). No smoothing functions or additional spectral manipulations were employed. Scanning electron microscopy was performed in an FEI Magellan 400L XHR SEM operating in magnetic immersion mode (TLD detector) at 10 kV and 50 pA at a working distance of 4.0 mm and without beam deceleration. The samples were the same as those used to acquire FTIR spectra (intrinsic Si substrates). The samples were stored in the glovebox for at most a few hours between FTIR measurement and SEM imaging. They were mounted to an SEM stub with carbon paint, transferred through air to the SEM, and imaged in vacuum without additional treatment (no conductive coating, plasma cleaning, etc.). Optical microscope images were acquired on an Olympus BX53M microscope with an SC50 camera. Proton NMR spectra of the PBG (700 μL of ~15 mM PBG in DMSO-d_6) were acquired on a Bruker DRX500 spectrometer with a BBO probe as standard. The optical absorptivity spectrum of PBG was collected on a PerkinElmer Lambda 950 spectrophotometer using a 100 μM solution of the PBG in EG measured in a quartz cuvette (1 cm path length).

FTIR Mapping. FTIR extinction spectra were mapped in a 5 × 5 rectangular grid (Δx = 2.9 mm, Δy = 3.625 mm) using an FTIR microscope with a 910 μm diameter spot (0.65 mm^2). The sample chamber was purged with flowing N$_2$ to minimize chemical deterioration of the film during the measurements. The microscope consisted of the Nicolet 6700 spectrometer outfitted with a homemade xy microscopy stage that utilized a ZnSe objective lens (6 mm focal length, Edmund Optics) and a plano-convex CaF$_2$ collimating lens (20 mm focal length, Thorlabs). Each grid point of the FTIR map was subsequently imaged by SEM and optical microscopy for densification and substrate coverage corrections, respectively, as per the oleate removal quantification process outlined in Figure S2.

Machine Learning SEM Image Analysis. Approximately 10 high-resolution (1.5 pixels/nm) images were acquired and analyzed for each film processing condition and sample type. QDs within the image were identified using the Laplacian of Gaussian (LoG) blob detection algorithm in the SciKit-image package. Voronoi decomposition was performed using the SciPy library. The following structural parameters were determined for each QD in the image: the number of nearest neighbors (NNs) in the Voronoi cell, the average NN distance, Ψ_4, Ψ_6, $\arg(\sin(\Psi_4))$, and $\arg(\cos(\Psi_4))$. Here,

$$\Psi_a = \frac{1}{p} \sum_j p_j e^{ai\phi_j}$$

where p is the total perimeter of the Voronoi cell, p_j is the edge length of the Voronoi cell with neighbor j, a is the bond-order parameter (4 or 6), i is the imaginary unit, and ϕ_j is the angle between the central QD and neighbor j with respect to the horizontal. The six structural metrics were assembled into a design matrix and input into a density-based spatial clustering algorithm (DBSCAN; SciKit-Learn package) that classified QDs based on their local SL structure. This clustering algorithm produced an arbitrary number of particle classes that were then color-coded on the SEM image. QDs at defect sites (e.g., grain

boundaries) were excluded from the reported Ψ_4 values. Inter-QD distances (d), density increase, and area per QD were extracted from fast Fourier transforms (FFTs) of the SEM images.

SEM Image Analysis for Extended Defect Quantification. Low-magnification SEM images (452 μm^2 fields of view) were acquired at random spots of multiple films made by piperidine injection and photobase illumination. Films were made as per Figure 4. In brief, the injection-made films were fabricated by injection of 0.5 mL of 11 mM piperidine in EG followed by a 1 h ligand exchange, while the photobase-made films were fabricated by illuminating 1 mM PBG in the EG for 1 h followed by 4 h of exchange in the dark. The intraflake cracks in each image were identified in ImageJ by contrast thresholding and subsequently corrected by detailed manual inspection. Total intraflake crack area and overall film coverage were calculated in ImageJ. The cracks were counted manually. Corresponding high-magnification images (0.72 μm^2 fields of view) were acquired at the same random spots for manual nanotear and chain split counting.

ASSOCIATED CONTENT

ⓢ Supporting Information

The Supporting Information is available free of charge at https://pubs.acs.org/doi/10.1021/acsnano.1c11130.

> FTIR and SEM data, fitting procedures, determination of percent oleate removed, pK_b values, image analysis process, characterization of the PBG molecule, maps of oleate removal, inter-QD distance and other parameters, results of control experiments, SEM defect analysis, and photograph of the setup for photobase-triggered epi-SL formation (PDF)

AUTHOR INFORMATION

Corresponding Author

Matt Law — *Department of Chemical and Biomolecular Engineering, University of California, Irvine, Irvine, California 92697, United States; Department of Materials Science and Engineering and Department of Chemistry, University of California, Irvine, Irvine, California 92697, United States;* ⓘ orcid.org/0000-0001-7645-9908; Email: matt.law@uci.edu

Authors

Caroline Qian — *Department of Chemical and Biomolecular Engineering, University of California, Irvine, Irvine, California 92697, United States*

Alex Abelson — *Department of Materials Science and Engineering, University of California, Irvine, Irvine, California 92697, United States*

Anneka Miller-Casas — *Department of Chemistry, University of California, Irvine, Irvine, California 92697, United States*

Robert Capp — *Department of Chemistry, University of California, Irvine, Irvine, California 92697, United States*

Ilya Vinogradov — *Department of Chemistry, University of California, Irvine, Irvine, California 92697, United States*

Nina S. Udagawa — *Department of Chemistry, University of California, Irvine, Irvine, California 92697, United States*

Nien-Hui Ge — *Department of Chemistry, University of California, Irvine, Irvine, California 92697, United States;* ⓘ orcid.org/0000-0002-0011-0790

Complete contact information is available at:
https://pubs.acs.org/10.1021/acsnano.1c11130

Author Contributions

C.Q. synthesized the QDs, fabricated the SLs, and collected/analyzed all data for the study. A.A. conceived the photobase generator concept, created the machine learning program to calculate Ψ_4, and assisted with SEM image analysis. R.C. assisted with FTIR spectroscopy. A.M.-C. performed the FTIR mapping, and I.V. and N.S.U. built the FTIR microscopy stage under the direction of N.-H.G. M.L. directed the study and assisted with data interpretation. C.Q. and M.L. wrote the manuscript with input from all authors.

Notes

The authors declare no competing financial interest.

REFERENCES

(1) Deveaud, B.; Shah, J.; Damen, T. C.; Lambert, B.; Regreny, A. Bloch transport of electrons and holes in superlattice minibands: direct measurement by subpicosecond luminescence spectroscopy. *Phys. Rev. Lett.* **1987**, *58*, 2582−2585.

(2) Remacle, F.; Levine, R. D. Quantum dots as chemical building blocks: elementary theoretical considerations. *ChemPhysChem* **2001**, *2*, 20−36.

(3) Jiang, C.-W.; Green, M. A. Silicon Quantum Dot Superlattices: Modeling of energy bands, densities of states, and mobilities for silicon tandem solar cell applications. *J. Appl. Phys.* **2006**, *99*, 114902.

(4) Kalesaki, E.; Evers, W. H.; Allan, G.; Vanmaekelbergh, D.; Delerue, C. Electronic structure of atomically coherent square semiconductor superlattices with dimensionality below two. *Phys. Rev. B* **2013**, *88*, 115431.

(5) Baumgardner, W. J.; Whitham, K.; Hanrath, T. Confined-but-connected quantum solids via controlled ligand displacement. *Nano Lett.* **2013**, *13*, 3225−3231.

(6) Evers, W. H.; Goris, B.; Bals, S.; Casavola, M.; de Graaf, J.; van Roij, R.; Dijkstra, M.; Vanmaekelbergh, D. Low-dimensional semiconductor superlattices formed by geometric control over nanocrystal attachment. *Nano Lett.* **2013**, *13*, 2317−2323.

(7) Sandeep, C. S. S.; Azpiroz, J. M.; Evers, W. H.; Boehme, S. C.; Moreels, I.; Kinge, S.; Siebbeles, L. D. A.; Infante, I.; Houtepen, A. J. Epitaxially connected PbSe quantum-dot films: controlled neck formation and optoelectronic properties. *ACS Nano* **2014**, *8*, 11499−11511.

(8) Kalesaki, E.; Delerue, C.; Morais Smith, C.; Beugeling, W.; Allan, G.; Vanmaekelbergh, D. Dirac cones, topological edge states, and nontrivial flat bands in two-dimensional semiconductors with a honeycomb nanogeometry. *Phys. Rev. X* **2014**, *4*, 011010.

(9) Whitham, K.; Yang, J.; Savitzky, B. H.; Kourkoutis, L. F.; Wise, F.; Hanrath, T. Charge transport and localization in atomically coherent quantum dot solids. *Nat. Mater.* **2016**, *15*, 557−563.

(10) Gómez-Campos, F. M.; Rodríguez-Bolívar, S.; Califano, M. High-mobility toolkit for quantum dot films. *ACS Photonics* **2016**, *3*, 2059−2067.

(11) Abelson, A.; Qian, C.; Salk, T.; Luan, Z.; Fu, K.; Zheng, J.-G.; Wardini, J. L.; Law, M. Collective topo-epitaxy in the self-assembly of a 3D quantum dot superlattice. *Nat. Mater.* **2020**, *19*, 49−55.

(12) Dong, A.; Chen, J.; Vora, P. M.; Kikkawa, J. M.; Murray, C. B. Binary nanocrystal superlattice membranes self-assembled at the liquid−air interface. *Nature* **2010**, *466*, 474−477.

(13) Weidman, M. C.; Smilgies, D.-M.; Tisdale, W. A. Kinetics of the self-assembly of nanocrystal superlattices measured by real-time *in situ* x-ray scattering. *Nat. Mater.* **2016**, *15*, 775−781.

(14) Boles, M. A.; Engel, M.; Talapin, D. V. Self-assembly of colloidal nanocrystals: from intricate structures to functional materials. *Chem. Rev.* **2016**, *116*, 11220−11289.

(15) Boneschanscher, M. P.; Evers, W. H.; Geuchies, J. J.; Altantzis, T.; Goris, B.; Rabouw, F. T.; van Rossum, S. A. P.; van der Zant, H. S. J.; Siebbeles, L. D. A.; Tendeloo, G. V.; Swart, I.; Hilhorst, J.; Petukhov, A. V.; Bals, S.; Vanmaekelbergh, D. Long-range orientation and atomic attachment of nanocrystals in 2D honeycomb super-lattices. *Science* **2014**, *344*, 1377−1380.

(16) Balazs, D. M.; Matysiak, B. M.; Momand, J.; Shulga, A. G.; Ibanez, M.; Kovalenko, M. V.; Kooi, B. J.; Loi, M. A. Electron mobility of 24 cm^2 V$^{−1}$ s$^{−1}$ in PbSe colloidal-quantum-dot superlattices. *Adv. Mater.* **2018**, *30*, 1802265.

(17) Anderson, N. C.; Hendricks, M. P.; Choi, J. J.; Owen, J. S. Ligand exchange and the stoichiometry of metal chalcogenide nanocrystals: spectroscopic observation of facile metal-carboxylate displacement and binding. *J. Am. Chem. Soc.* **2013**, *135*, 18536−18548.

(18) Walravens, W.; De Roo, J.; Drijvers, E.; ten Brinck, S.; Solano, E.; Dendooven, J.; Detavernier, C.; Infante, I.; Hens, Z. Chemically triggered formation of two-dimensional epitaxial quantum dot superlattices. *ACS Nano* **2016**, *10*, 6861−6870.

(19) Suyama, K.; Shirai, M. Photobase generators: Recent progress and application trend in polymer systems. *Prog. Polym. Sci.* **2009**, *34*, 194−209.

(20) Kim, W. J.; Kim, S. J.; Lee, K.-S.; Samoc, M.; Cartwright, A. N.; Prasad, P. N. Robust microstructures using UV photopatternable semiconductor nanocrystals. *Nano Lett.* **2008**, *8*, 3262−3265.

(21) Wang, Y.; Fedin, I.; Zhang, H.; Talapin, D. V. Direct optical lithography of functional inorganic nanomaterials. *Science* **2017**, *357*, 385−388.

(22) Cho, H.; Pan, J.-A.; Wu, H.; Lan, X.; Coropceanu, I.; Wang, Y.; Cho, W.; Hill, E. A.; Anderson, J. S.; Talapin, D. V. Direct optical patterning of quantum dot light-emitting diodes via in situ ligand exchange. *Adv. Mater.* **2020**, *32*, 2003805.

(23) Yang, J.; Hahm, D.; Kim, K.; Rhee, S.; Lee, M.; Kim, S.; Chang, J. H.; Park, H. W.; Lim, J.; Lee, M.; Kim, H.; Bang, J.; Ahn, H.; Cho, J. H.; Kwak, J.; Kim, B.; Lee, C.; Bae, W. K.; Kang, M. S. High-resolution patterning of colloidal quantum dots via non-destructive, light-driven ligand crosslinking. *Nat. Commun.* **2020**, *11*, 2874.

(24) Gao, Y.; Huang, J.-T.; Balazs, D. M.; Xu, Y.; Hanrath, T. Photoinitiated transformation of nanocrystal superlattice polymorphs assembled at a fluid interface. *Adv. Mater. Interfaces* **2020**, *7*, 2001064.

(25) Nuchnapa, T.; Pakdeewanishsukho, K.; Jamieson, A.; Sirivat, A.; Wongkasemjit, S. Electrical properties of a novel lead alkoxide precursor: Lead glycolate. *Mater. Chem. Phys.* **2006**, *98*, 138−143.

(26) Lynch, C. T.; Mazdiyasni, K. S.; Smith, J. S.; Crawford, W. J. Infrared spectra of transition metal alkoxides. *Anal. Chem.* **1964**, *36*, 2332−2337.

(27) Kundu, K. K.; Das, M. N. Autoprotolysis constants of ethylene glycol and propylene glycol and dissociation constants of some acids and bases in the solvents at 30 °C. *J. Chem. Eng. Data* **1964**, *9*, 82−86.

(28) *The Merck Index - An Encyclopedia of Chemicals, Drugs, and Biologicals*, 15th ed.; O'Neil, M. J., Ed.; Royal Society of Chemistry: Cambridge, UK, 2013.

(29) *CRC Handbook of Chemistry and Physics*, 100th ed.; Rumble, J. R., Ed.; CRC Press: Boca Raton, FL, 2019.

(30) Bates, R. G. Solute-solvent interactions and acid-base dissociation in mixed solvent systems. *J. Electroanal. Chem. Interfacial Electrochem.* **1971**, *29*, 1−19.

(31) Breant, M.; Arnaud, N.; Desmettre, S. Spectrophotometric determination of the pH scale in ethane-1,2-diol. *Anal. Chim. Acta* **1979**, *104*, 181−183.

(32) Hulanicki, A.; Głab, S. Coulometric titrations in microscale study of ionic equilibria. *Fresenius J. Anal. Chem.* **1990**, *337*, 512−517.

(33) Zarghami, M. H.; Liu, Y.; Gibbs, M.; Gebremichael, E.; Webster, C.; Law, M. p-Type PbSe and PbS quantum dot solids prepared with short-chain acids and diacids. *ACS Nano* **2010**, *4*, 2475−2485.

(34) Balazs, D. M.; Dirin, D. N.; Fang, H.-H.; Protesescu, L.; ten Brink, G. H.; Kooi, B. J.; Kovalenko, M. V.; Loi, M. A. Counterion-mediated ligand exchange for PbS colloidal quantum dot superlattices. *ACS Nano* **2015**, *9*, 11951−11959.

(35) Halperin, B. I.; Nelson, D. R. Theory of two-dimensional melting. *Phys. Rev. Lett.* **1978**, *41*, 121−124.

(36) Kumar, V. S.; Kumaran, V. Bond-orientational analysis of hard-disk and hard-sphere structures. *J. Chem. Phys.* **2006**, *124*, 204508.

(37) McCray, A. R. C.; Savitzky, B. H.; Whitham, K.; Hanrath, T.; Kourkoutis, L. F. Orientational disorder in epitaxially connected quantum dot solids. *ACS Nano* **2019**, *13*, 11460−11468.